

Gate-controlled spin filter, spin valve, and negative differential resistance in cold metal/bipolar magnetic semiconductor lateral homologous heterojunctions

Zhao Chen

Department of Physics, Hefei University of Technology, Hefei, Anhui 230009, China

Xingxing Li *

Key Laboratory of Precision and Intelligent Chemistry, University of Science and Technology of China, Hefei, Anhui 230026, China and Hefei National Research Center for Physical Sciences at the Microscale, University of Science and Technology of China, Hefei, Anhui 230026, China



(Received 24 November 2023; revised 4 January 2024; accepted 5 February 2024; published 26 February 2024)

Achieving multifunctional integration in two dimensions is highly desired for developing next-generation nanoelectronic devices but remains a challenge. Here, combining the advantages of cold metal and a bipolar magnetic semiconductor (BMS), three distinct functions, i.e., a spin filter, spin valve, and negative differential resistance, are simultaneously realized in a cold metal $2H\text{-TaS}_2$ /BMS $2H\text{-VS}_2$ /cold metal $2H\text{-TaS}_2$ lateral homologous heterojunction, where the BMS $2H\text{-VS}_2$ is controlled by two electric gates placed on the left and right parts. The spin filter and spin valve effects originate from the bipolar spin-polarized band structure of $2H\text{-VS}_2$, where its carriers' spin orientation can be easily flipped by shifting the Fermi level into either the valence or conduction band. Thus, in the junction, the current's spin polarization (spin up or spin down) and intensity (high or low conductance) can be switched by adjusting the polarities of the two applied gates: Once two gate voltages are both positive or negative, the junction works as a spin filter with either a fully spin-down or fully spin-up polarized current. While the two gate voltages possess opposite signs, the junction's current is prohibited due to mismatched spin orientations of carriers in the two parts of $2H\text{-VS}_2$, leading to the spin valve effect. At the same time, the intrinsic energy gaps around the Fermi level in cold metal $2H\text{-TaS}_2$ and the band-to-band tunneling of carriers from $2H\text{-TaS}_2$ to $2H\text{-VS}_2$ endow the junction with a significant negative differential resistance behavior with a large peak-to-valley current ratio.

DOI: [10.1103/PhysRevB.109.054428](https://doi.org/10.1103/PhysRevB.109.054428)

I. INTRODUCTION

Two-dimensional (2D) magnetic materials, showing great potential for enhancing the functionality and improving the integration density of electronic devices by utilizing the spin degree of freedom, have attracted extensive research interest [1–4]. Meanwhile, due to their isolated atomic planes, 2D magnetic materials exhibit great opportunities for gate tunability and integrated flexibility, which is desirable for next-generation functional spintronic devices [5–7]. In recent years, some atom-thick magnetic materials were discovered in experiments, such as FePS_3 [8], CrI_3 [9], $\text{Cr}_2\text{Ge}_2\text{Te}_2$ [10], Fe_3GeTe_2 [5], and MnSe_2 [11]. To develop high-performance nanospintronic devices, efficient and flexible control of the carriers' spin is required. In this aspect, bipolar magnetic semiconductors (BMSs), whose valence band (VB) and conduction band (CB) edges possess opposite spin channels, offer an ideal platform [12–15]. BMSs can be used to construct bipolar field-effect spin filters and spin valves [13,15]. In BMS-based bipolar field-effect spin filters, 100% spin-polarized currents with reversible spin orientation can be generated and controlled by simply applying a gate voltage

[12,13,16,17]. In BMS-based bipolar field-effect spin valves, the on and off states of the current can be switched by changing the polarities of two applied gates [13,18]. To date, several intrinsic 2D BMSs have been predicted by theoretical calculations, including monolayer $2H\text{-VS}_2$ and $2H\text{-VSe}_2$ [19,20], the 2D MnPSe_3 nanosheet [21], 2D metal-free B_4CN_3 [22], 2D metal-organic frameworks [17,23–31], and 2D cluster-assembled sheets $[\text{NH}_4]_3[\text{Fe}_6\text{S}_8(\text{CN})_6]\text{Cr}$ [32]. Encouragingly, high-quality $2H\text{-VS}_2$ single-crystal nanosheets have already been successfully synthesized [33,34]. In addition, room temperature ferromagnetism of monolayer $2H\text{-VS}_2$ has been experimentally confirmed [34].

Besides exploiting 2D magnetic materials, another route to improve the integration is to develop multiple-valued logic (MVL). MVL can transmit more information with fewer interconnect lines between devices than conventional binary logic by conveying multivalued signals. Thus, it has great potential to reduce the complexity of modern integrated circuit design [35,36]. In this aspect, the nonlinear fold-back $I\text{-V}$ characteristics of negative differential resistance (NDR) devices serve as a promising way to realize MVL applications [37–39]. Various schemes for achieving the NDR property in Esaki diodes [40,41], resonant tunneling diodes [42–45], Gunn diodes [46,47], single-electron transistors [48,49], and molecular devices [50,51] have been researched. In particular,

*lix@ustc.edu.cn

NDR behavior based on band-to-band tunneling mechanism remains a research hot topic. Band-to-band tunneling is the quantum tunneling of carriers through a tunneling window located between two semiconductor regions [52–54] in which NDR can be induced by a decrease in the available states of the tunnel current with the increase of bias voltage [40]. Along with the booming development of 2D van der Waals heterojunctions, different varieties of 2D heterojunctions exhibit NDR characteristics based on the band-to-band tunneling mechanism, such as $\text{MoS}_2/\text{WSe}_2$, $\text{WSe}_2/\text{SnSe}_2$, $\text{SnSe}_2/\text{MoTe}_2$, black phosphorus (BP)/ $\text{ReS}_2/\text{HfS}_2$, BP/ InSe , BP/ SnSe_2 , and BP/ ReS_2 [37,55–60]. However, the peak-to-valley current ratios (PVCRs) in these heterojunctions are usually lower than 10 at room temperature. Generally, a large PVCr is desirable for providing a wide range of middle states in MVL applications. Recently, it was predicted that using cold metal MX_2 ($M = \text{Nb}, \text{Ta}; X = \text{S}, \text{Se}$) [61–64] as an injection source would significantly improve the PVCr [65,66]. Cold metals, which have intrinsic gaps around the Fermi level and work like naturally p -type or n -type semiconductors [67], are an ideal solution to deliver a large PVCr owing to the relatively localized electrons around the Fermi level. As a typical cold metal, $2H\text{-TaS}_2$ has been extensively studied experimentally and theoretically [64–67].

In this work, by using the cold metal $2H\text{-TaS}_2$ and the bipolar magnetic semiconductor $2H\text{-VS}_2$, we construct a $2H\text{-TaS}_2/2H\text{-VS}_2/2H\text{-TaS}_2$ lateral homologous heterojunction, where $2H\text{-VS}_2$ is divided into two regions that are controlled by two different gates. The spin-polarized transport simulations of the heterojunction show that the spin filter, spin valve, and negative differential resistance effect can be realized simultaneously by changing the signs of the two gate voltages.

II. METHODS

The geometric and electronic structures of $2H\text{-TaS}_2$ and $2H\text{-VS}_2$ are calculated using the projector augmented wave method, within the framework of density functional theory (DFT) as implemented in the Vienna Ab initio Simulation Package (VASP) [68,69]. The exchange-correlation interaction between electrons is described within the generalized gradient approximation as parameterized by the Perdew-Burke-Ernzerhof functional [70]. The kinetic energy cutoff is set to 500 eV. A $15 \times 15 \times 1$ Monkhorst-Pack k mesh is used. An effective Hubbard term (Dudarev’s method) of $U_{\text{eff}} = 1$ eV is added in for the $3d$ orbitals of V, as adopted in a previous study [19]. The convergence criterion for the total energy in the electronic iteration is 1.0×10^{-5} eV. Geometry optimization is performed until the force acting on each atom is less than $0.01 \text{ eV}\text{\AA}^{-1}$.

The transport properties are explored by using the nonequilibrium Green’s function DFT method implemented in the Atomistic Simulation Toolkit (ATK) software package [71,72]. The on-site U correction is set to 1 eV for the V atom to include the $3d$ electrons’ correlation effects. The PSEUDODOJO pseudopotentials [73] with medium basis sets are adopted for Ta, V, and S atoms. The medium basis sets are generated by reducing the range of the original pseudoatomic orbitals, requiring that the change in DFT-obtained total energies does

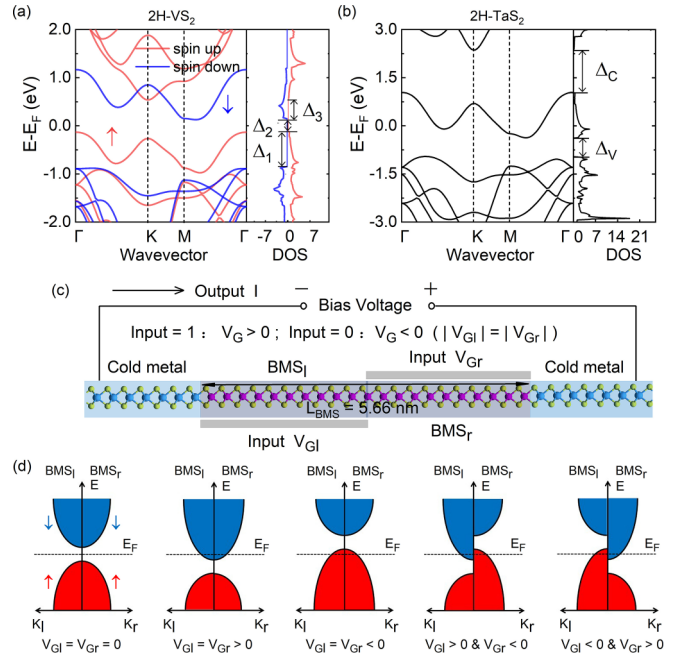


FIG. 1. Band structures (left panel) and density of states (DOS) (right panel) of (a) $2H\text{-VS}_2$ and (b) $2H\text{-TaS}_2$. The Fermi levels are set to zero. (c) The structure of the $2H\text{-TaS}_2/2H\text{-VS}_2/2H\text{-TaS}_2$ heterojunction device. (d) Schematic band structures for the left and right regions of the BMS channel with two gate voltages (V_{Gl} , V_{Gr}) applied. E_F is the Fermi level of BMS.

not exceed 4 meV/atom [74]. A kinetic energy cutoff of 100 hartrees is set for the real-space grid. The bulk rigid relaxation method implemented in ATK is adopted to optimize device configuration: The center region is extracted from the device with the right end of the unit cell extended by a vacuum region, as shown in Fig. S1 of the Supplemental Material (SM) [75]. Then, we fix the atoms of the left electrode extension and apply a rigid constraint to the atoms of the right electrode extension while other atoms are fully relaxed. Finally, the device is reassembled from the relaxed center region. In the self-consistent calculation, a k -point mesh of $13 \times 1 \times 180$ is used to calculate the Hamiltonian matrix and density matrix. To calculate transmission coefficients, a 51×1 k mesh is adopted.

VASP can support high computational accuracy for the structural and electronic properties of periodic systems, while the ATK package is ideally suited for dealing with electron transport calculations for nanoscale devices. It is generally accepted that the structural and electronic properties of periodic crystals are studied with VASP before ATK is used to investigate the electron transport of nanoscale devices [76,77]. Furthermore, we also use ATK to calculate the band structure of the $2H\text{-VS}_2$ monolayer, which is consistent with that calculated by VASP (as shown in Fig. S2 of the SM [75]).

III. RESULTS AND DISCUSSION

As shown in Fig. 1(a), the $2H\text{-VS}_2$ monolayer is a BMS with the VB and CB approaching the Fermi level through opposite spin channels [19]. There are three energy gaps, Δ_1 , Δ_2 , and Δ_3 , that describe the typical characteristics of BMS

materials. Δ_2 represents the spin-flip gap between VB and CB edges from opposite spin channels. Δ_1 and Δ_3 reflect spin splitting gaps in the VB and CB, respectively. For real applications, Δ_2 should be relatively small to ensure that it is feasible to generate carriers in different spin channels by adjusting the position of the Fermi level via moderate gate voltages [12]. The $2H$ - VS_2 monolayer has a narrow spin-flip gap Δ_2 of 0.26 eV, making it an excellent BMS material for gate-controlled spin transport [12,19].

The band structure of the cold metal $2H$ - TaS_2 is shown in Fig. 1(b). $2H$ - TaS_2 is a nonmagnetic metal, but unlike conventional metals, it has an isolated partially occupied band crossing the Fermi level, where an obvious energy gap Δ_V/Δ_C appears between the partially occupied band and its lower occupied VB/upper unoccupied CB band [65–67]. Thus, metallic $2H$ - TaS_2 can work like a naturally p -doped or n -doped semiconductor.

To gain insights into electronic structure changes in $2H$ - VS_2 and $2H$ - TaS_2 following device formation, we calculate the electrostatic potential and the projected band structure of the $2H$ - $VS_2/2H$ - TaS_2 lateral heterostructure (Fig. S3 of the SM [75]). The unit cell of the lateral heterostructure is presented in Fig. S3(c) of the SM [75]. The direction perpendicular to the interface of $2H$ - $VS_2/2H$ - TaS_2 is set as the Y direction. The plane-averaged electrostatic potential $V(Y)$ is represented by the oscillating black line. The oscillations can be further filtered with the macroscopic averaging technique as indicated by the red line, which is denoted as $\bar{V}(Y)$. The electrostatic potentials of the isolated $2H$ - VS_2 and $2H$ - TaS_2 are also presented in Figs. S3(a) and S3(b) of the SM [75]. $\bar{V}(Y)$ is flat, with a value of 0 eV in both isolated $2H$ - VS_2 and $2H$ - TaS_2 structures. For the $2H$ - $VS_2/2H$ - TaS_2 heterostructure, $\bar{V}(Y)$ is nearly flat in the left $2H$ - VS_2 region, with a value of -0.09 eV, and the right $2H$ - TaS_2 region, with a value of 0.07 eV, but increases smoothly and linearly across the interface. It is in agreement with the behavior of metal-semiconductor junctions [78,79]. The projected band structures show that $2H$ - TaS_2 and $2H$ - VS_2 basically retain their intrinsic electronic characteristics in the $2H$ - $TaS_2/2H$ - VS_2 heterostructure: There is an obvious energy gap above and under the Fermi level in cold metal $2H$ - TaS_2 bands, and the valence and conduction bands of $2H$ - VS_2 carry opposite spin polarizations. Due to the slight hybridization between $2H$ - TaS_2 and $2H$ - VS_2 , the spin-flip gap Δ_2 of $2H$ - VS_2 is reduced from 0.26 to 0.24 eV. The valence band maximum in the spin-up channel is closer to the Fermi level than the conduction band minimum in the spin-down channel. This indicates that the spin-up carriers would contribute a greater current than the spin-down carriers when a small bias voltage is applied.

The structure of the lateral heterojunction device built with the cold metal $2H$ - TaS_2 and the BMS $2H$ - VS_2 is illustrated in Fig. 1(c): the left and right metallic $2H$ - TaS_2 are used as electrodes, and the middle channel is composed of the BMS $2H$ - VS_2 , which is further divided into two regions with two different applied gates. In the relaxed heterojunction device, the V-S and Ta-S bond lengths are 2.38 and 2.45 Å at the interface, respectively. The lengths of the V-S and Ta-S bonds far from the interface are the same as those in the $2H$ - VS_2 and $2H$ - TaS_2 monolayers, which are 2.37 and 2.48 Å, respectively.

The V-S bond is slightly stretched, and the Ta-S bond is compressed at the interface. The two gate voltages are labeled V_{G1} and V_{G2} . For simplicity, here, we consider only $|V_{G1}| = |V_{G2}|$. Figure 1(d) shows a schematic plot of the band shift for the left and right regions of the BMS channel with the change in the two gate voltages (V_{G1} , V_{G2}). At $V_{G1} = V_{G2} = 0$, the Fermi levels of the left and right regions of the BMS are both in the spin-flip gap Δ_2 , leading to an output current of almost zero. When $V_{G1} = V_{G2} < 0$, both Fermi levels of the two regions of the BMS channel shift down into spin splitting gap Δ_1 , which induces BMS channel conductance with completely spin-up polarized carriers and currents. If $V_{G1} = V_{G2} > 0$, both Fermi levels move up into spin splitting gap Δ_3 , and the conducting carriers and currents change to fully spin down polarized [12,13]. At $V_{G1} > 0$ and $V_{G2} < 0$, the Fermi level of left BMS moves up, and that of the right BMS shifts down, which produces completely spin-down carriers in the left region and spin-up carriers in the right region of the BMS. Conversely, $V_{G1} < 0$ and $V_{G2} > 0$ result in completely spin-up carriers in the left region and spin-down carriers in the right region of the BMS. In these two cases, conduction carriers in the two regions of the BMS channel are mismatched in spin orientation, leading to nearly vanishing currents, i.e., the off state. To sum up, once the signs of the two gate voltages are both negative or positive, a completely spin-up or spin-down current is generated, which realizes the function of a spin filter. Furthermore, the on/off state of the heterojunction can be switched by applying same- or opposite-sign gate voltages, which equates to the function of a spin valve.

The above analyses are confirmed by our transport simulations of the heterojunction. The calculated spin-resolved current vs bias voltage $I - V_b$ curves under different gate voltages are illustrated in Fig. 2. It is found that with two positive gate voltages, $V_{G1} = V_{G2} = 1$ V, the spin-down current (blue line) passing through the heterojunction is remarkably larger than the spin-up current (red line). Obviously, at each bias voltage, the spin-up currents are almost zero, leading to a 100% spin-down polarization. For example, the spin-up and spin-down currents are 1.2×10^{-6} and 1.1×10^{-2} μ A, respectively, under a bias voltage of 0.15 V. On the other hand, with two negative gate voltages ($V_{G1} = V_{G2} = -1$ V), the spin-down currents are nearly zero, which results in a 100% spin-up polarization. For instance, under a bias voltage of 0.15 V, the spin-up and spin-down currents are 2.4×10^{-1} and 1.5×10^{-7} μ A, respectively. When the two gate voltages have different signs ($V_{G1} = 1$ and $V_{G2} = -1$ V or $V_{G1} = -1$ and $V_{G2} = 1$ V), the spin-up and spin-down currents are both nearly zero for bias voltage ranging from 0 to 0.15 V. Note that when the bias voltage increases to 0.2 V or higher, the current under $V_{G1} = 1$ and $V_{G2} = -1$ V becomes significant, which will be discussed later. Above all, completely spin-polarized currents with reversible spin polarization and the on/off state, i.e., the spin filter and spin valve, can be achieved simultaneously in the heterostructure by tuning the signs of two applied gate voltages. Figure 2(e) gives the truth table of the BMS-based spin valve. Furthermore, we calculate the ratio of on-state to off-state currents of the spin valve with the increase of two gate voltages. The on/off ratio is calculated as I_{++}/I_{-+} at a bias voltage of 0.45 V or I_{--}/I_{-+} at a bias voltage of 0.3 V, where I_{++} , I_{--} , and I_{-+} are the total

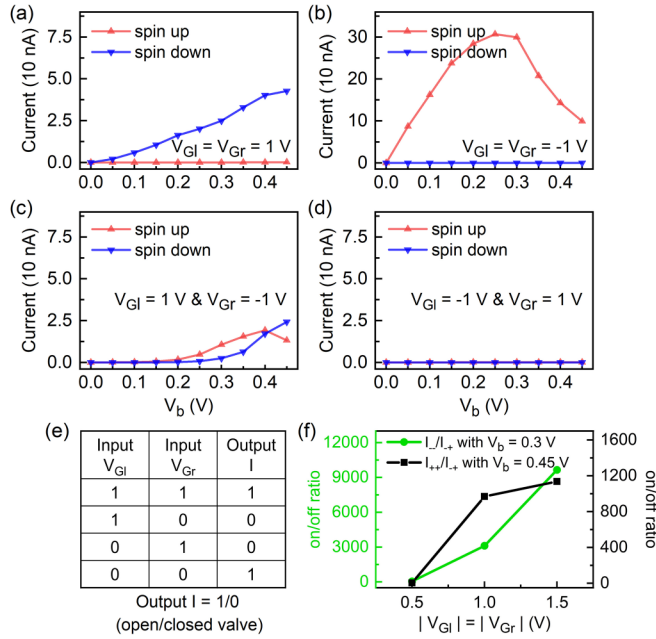


FIG. 2. The spin-resolved current vs bias voltage $I - V_b$ curves under different gate voltages: (a) $V_{GI} = V_{Gr} = 1$ V, (b) $V_{GI} = V_{Gr} = -1$ V, (c) $V_{GI} = 1$ and $V_{Gr} = -1$ V, and (d) $V_{GI} = -1$ and $V_{Gr} = 1$ V. (e) Truth table of the BMS field-effect spin valve. (f) The value of the on/off ratio under different gate voltages. I_{++} , I_{--} , and I_{+-} are the total currents with two gate voltages of $V_{GI} = V_{Gr} > 0$, $V_{GI} = V_{Gr} < 0$, and $V_{GI} < 0$ and $V_{Gr} > 0$, respectively.

currents for $V_{GI} = V_{Gr} > 0$, $V_{GI} = V_{Gr} < 0$, and $V_{GI} < 0$ and $V_{Gr} > 0$, respectively. As shown in Fig. 2(f), the on/off ratio increases significantly with the increase of gate voltages, with the maximum value reaching 10^4 .

To gain insight into the mechanism of manipulating spin-polarized currents through the heterojunction, we present the zero-bias transmission spectra under different gate voltages in Figs. 3(a), 3(c), 3(e), and 3(g). The zero-bias transmission spectrum without gate voltages is shown in Fig. S4(a) of the SM [75]. By applying two positive gate voltages, the transmission peaks of both spin channels move down to the low-energy region. With $V_{GI} = V_{Gr} = 1$ V [Fig. 3(a)], the peak contributed by the perturbed spin-down CB of $2H-VS_2$ is just above the Fermi level, while the peak contributed by the perturbed spin-up VB is away from the Fermi level by -0.33 eV. When the bias voltage ranges from 0 to 0.15 eV, only the transmission peak contributed by the spin-down CB resides in the bias window, resulting in a spin-down on state of the heterojunction. When two gate voltages are negative, the transmission peaks of both spin channels move up to the high-energy region. With $V_{GI} = V_{Gr} = -1$ V [Fig. 3(c)], the transmission peak contributed by the perturbed spin-up VB crosses the Fermi level, while the spin-down CB peak is 0.35 eV away. With a bias voltage from 0 to 0.15 eV, the spin-up VB always makes the dominant contribution to the electron transport, leading to a spin-up on state of the heterojunction.

When two applied gate voltages have opposite signs, e.g., $V_{GI} = 1$ and $V_{Gr} = -1$ V, all transmission peaks of the left $2H-VS_2$ part shift to the low-energy region, while the right $2H-VS_2$ part moves to the high-energy region. Thus, the

carriers' spin polarization directions in the left and right $2H-VS_2$ regions will be mismatched. Consequently, there are no spin-up and spin-down transmission peaks in the energy range from -0.20 to 0.27 eV for $V_{GI} = 1$ and $V_{Gr} = -1$ V and $V_{GI} = -1$ and $V_{Gr} = 1$ V, as shown in Figs. 3(e) and 3(g). When the bias voltage is in the range from 0 to 0.15 V, the two spin channels are both blocked, which leads to an off state of the heterojunction.

In order to further demonstrate the gate control of the spin transport, the spin- and spatially resolved projected local density of states (PLDOS) along the transport direction at different gate voltages is calculated and shown in Figs. 3(b), 3(d), 3(f), and 3(h). The PLDOS without gate voltages is presented in Fig. S4(b) of the SM [75]. From top to bottom and left to right, the PLDOS shows the electronic states arranged according to their energies and spatial locations, respectively. The device's Fermi level is set to zero. Light yellow denotes the spin-up and spin-down electronic states, while black indicates no electronic states exist. It is clear that at $V_{GI} = V_{Gr} = 1$ V, the spin-down CB in the channel region is located just above the Fermi level, while all the spin-up states remain far away; hence, the spin-down electrons dominate the transport. At $V_{GI} = V_{Gr} = -1$ V, the channel's spin-up VB passes through the Fermi level, with all spin-down states far away; thus, only spin-up electrons can transmit. At $V_{GI} = 1$ and $V_{Gr} = -1$ V, all states of the left $2H-VS_2$ channel are below those of the right $2H-VS_2$ channel, with only the spin-up VB of the right $2H-VS_2$ channel crossing the Fermi level, which suggests that no electrons can pass through at low bias voltage. For $V_{GI} = -1$ and $V_{Gr} = 1$ V, only the spin-up VB of the left $2H-VS_2$ channel crosses the Fermi level, and again, electron transport through the whole heterojunction is blocked.

It is worth noting that the off state at $V_{GI} = 1$ and $V_{Gr} = -1$ V will be switched to the on state with the increase of bias voltage [Fig. 2(c)]. As a comparison, the off state at $V_{GI} = -1$ and $V_{Gr} = 1$ V can remain within the considered bias voltage [Fig. 2(d)]. In our calculations, the left electrode is applied with negative bias voltage, $-\frac{1}{2}V_b$, while the right electrode is applied with positive bias voltage, $+\frac{1}{2}V_b$. Under such bias voltage, electron carriers are transferred from the left electrode to right electrode. At $V_{GI} = 1$ and $V_{Gr} = -1$ V, all the spin-up and spin-down energy levels of the left $2H-VS_2$ channel are below those of the right $2H-VS_2$ channel [Fig. 3(i)]. The spin-up VB of the left $2H-VS_2$ channel is below the Fermi level, and that of the right $2H-VS_2$ channel is just above the Fermi level. Consequently, to pass through the junction, spin-up electron carriers need to overcome the energy gap between the left and right $2H-VS_2$ channels. Similarly, for spin-down electrons, an energy gap also exists between the left and right $2H-VS_2$ channels. In addition, because the spin-down CB is located above the Fermi level, an energy barrier emerges between the left electrode and left $2H-VS_2$ channel. Under the action of bias voltage (counteracted by the gate voltage), all the energy levels of the left channel move up, and those of the right channel move down. The energy gap between the left and right channels will gradually disappear with the increase in bias voltage [Fig. 3(i)]. Simultaneously, the spin-down energy barrier between the left electrode and left $2H-VS_2$ channel will become thinner step by step [80,81]. Thus, with a large bias voltage,

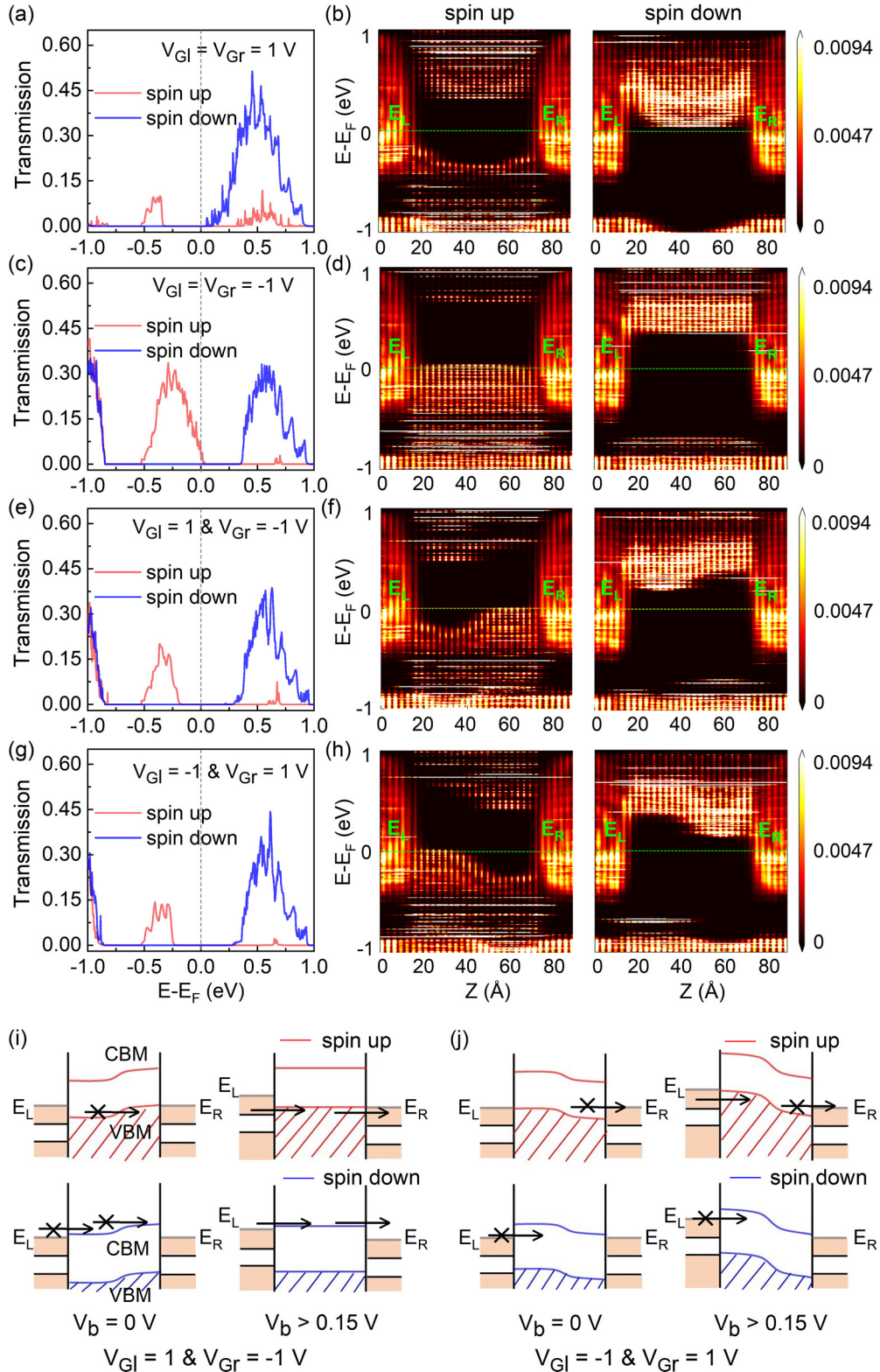


FIG. 3. The zero-bias transmission spectra of the $2H$ -TaS₂/ $2H$ -VS₂/ $2H$ -TaS₂ heterojunction under different gate voltages: (a) $V_{Gl} = V_{Gr} = 1$ V, (c) $V_{Gl} = V_{Gr} = -1$ V, (e) $V_{Gl} = 1$ and $V_{Gr} = -1$ V, and (g) $V_{Gl} = -1$ and $V_{Gr} = 1$ V. Here, the blue and red lines stand for the spin-down and spin-up channels, respectively. The spin- and spatially resolved projected local density of states (PLDOS) under different gate voltages: (b) $V_{Gl} = V_{Gr} = 1$ V, (d) $V_{Gl} = V_{Gr} = -1$ V, (f) $V_{Gl} = 1$ and $V_{Gr} = -1$ V, and (h) $V_{Gl} = -1$ and $V_{Gr} = 1$ V. Schematic band diagrams with different bias voltages (left panel for $V_b = 0$ V and right panel for $V_b > 0.15$ V) with (i) $V_{Gl} = 1$ and $V_{Gr} = -1$ V and (j) $V_{Gl} = -1$ and $V_{Gr} = 1$ V. E_L and E_R are the Fermi levels of the left and right electrodes, respectively. VBM and CBM are the valence band maximum and conduction band minimum, respectively. The arrow indicates the direction of electron transport.

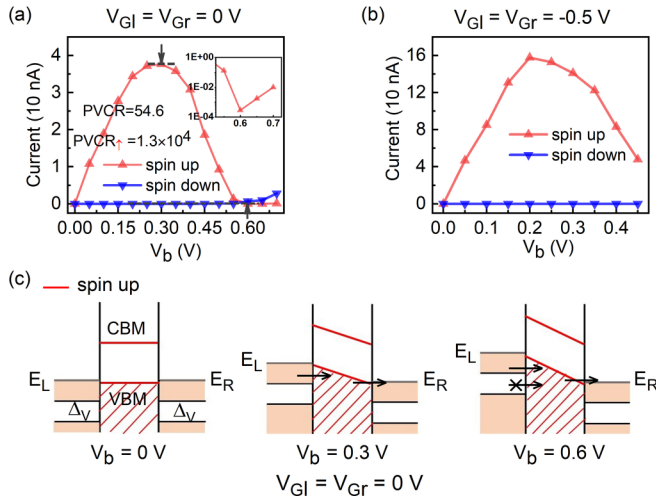


FIG. 4. The spin-resolved current vs bias voltage $I - V_b$ curves under different gate voltages: (a) $V_{Gl} = V_{Gr} = 0$ V and (b) $V_{Gl} = V_{Gr} = -0.5$ V. (c) Schematic band diagrams under different bias voltages ($V_b = 0, 0.3, 0.6$ V) with $V_{Gl} = V_{Gr} = 0$ V. E_L and E_R are the Fermi levels of the left and right electrodes, respectively. VBM and CBM are the valence band maximum and conduction band minimum, respectively. The arrow indicates the direction of electron transport.

the spin-up VB and spin-down CB both make a dominant contribution to the transmission, resulting in the on state. At $V_{Gl} = -1$ and $V_{Gr} = 1$ V, all spin-up and spin-down energy levels of the left channel are above those of the right channel [Fig. 3(j)]. The spin-up VB of the left channel just crosses the Fermi level, and that of the right channel is far below the Fermi level, leading to an energy barrier between the right channel and right electrode in spin-up electron transmission. At the same time, because the left channel's spin-down CB is far above the Fermi level, a large energy barrier occurs between the left electrode and left channel in spin-down electron transmission. With the increase in bias voltage (which cooperates with the gate voltage), the spin-up and spin-down energy levels of the left channel become higher than those of the right channel. In this case, significant energy barriers still exist in both the spin-up and spin-down channels. Hence, the two spin channels remain blocked [Fig. 3(j)]. The calculated PLDOS and transmission spectrum further confirm this picture (Fig. S5 of the SM [75]).

Obviously, when the two gate voltages are $V_{Gl} = V_{Gr} = -1$ V, the NDR phenomenon is observed in the $I - V_b$ curve [Fig. 2(b)]. To further confirm the NDR effect, we also calculate the $I - V_b$ curves at $V_{Gl} = V_{Gr} = 0$ V and $V_{Gl} = V_{Gr} = 0.5$ V [Figs. 4(a) and 4(b)]. The results imply that at zero and negative gate voltages, the dominating spin-up current passing through the heterojunction first increases and then decreases with the increase in the bias voltage, showing a typical NDR effect. Moreover, a large peak-to-valley spin-up current ratio and total current ratio of 1.3×10^4 and 54.6 are achieved, respectively. To understand such NDR behavior, we give the band alignments for the spin-up channel of the heterojunction varied with bias voltage V_b in Fig. 4(c). At $V_b = 0$ V, the energy gap Δ_V in the cold metal $2H$ -TaS₂

locates below the valence band maximum (VBM) of $2H$ -VS₂. When a small bias voltage is applied ($0 < V_b < 0.3$ V), the current increases because more electron carriers from the left $2H$ -TaS₂ electrode tunnel into the VB states of the $2H$ -VS₂ channel. The current continuously increases until the top edge of the energy gap Δ_V of the left $2H$ -TaS₂ electrode aligns with the Fermi level of the right $2H$ -TaS₂ electrode. At this critical point ($V_b = 0.3$ V), the filled states in the left $2H$ -TaS₂ are maximally overlapped in energy with states of the $2H$ -VS₂ channel, resulting in a maximum current (peak current). Further increasing the bias voltage ($0.3 < V_b < 0.6$ V) leads to a decrease in the current. At $V_b = 0.6$ V, the current comes to the valley point. On the other hand, the spin-down current always has a low value, with $0 < V_b < 0.6$ V. When a high bias voltage is applied ($V_b > 0.6$ V), the energy barrier between the left electrode and left channel will become thinner, and the spin-down CB will cross the Fermi level of the left electrode and enter the bias window (Fig. S6 of the SM [75]). Meanwhile, the Fermi level of the right electrode gets close to the bottom edge of the energy gap Δ_V of the left electrode. Thus, the current increases again as a result of the enhanced electron tunneling and thermionic emission. The calculated PLDOS and transmission spectra further confirm this picture (Figs. S6 and S7 of the SM [75]). Consequently, a significant NDR effect with a large PVCR is realized.

Overall, the proposed $2H$ -TaS₂/ $2H$ -VS₂/ $2H$ -TaS₂ lateral heterojunction has the following four significant achievements and advantages: First, we developed a spintronic lateral heterojunction based on transition metal dichalcogenides, while previous studies mostly focused on their optical and electrical properties [65,66,82,83]. Second, this spintronic heterojunction is expected to work at room temperature and can easily be synthesized by employing the mature and popular in-plane epitaxial growth technique [82,84,85]. Third, three distinct functions, i.e., the spin valve, spin filter, and negative differential resistance, are simultaneously integrated into the spintronic heterojunction. Finally, fully electrical manipulation of these three spintronic functions was realized.

IV. CONCLUSION

In conclusion, the present study proposed a cold metal $2H$ -TaS₂/bipolar magnetic semiconductor $2H$ -VS₂/cold metal $2H$ -TaS₂ lateral homologous heterojunction, where $2H$ -VS₂ is divided into two regions and controlled by two different gate voltages. The spin-polarized electronic transport simulations showed that the on/off state of the current in the heterojunction is achievable by applying two gates with the same/opposite polarity. Furthermore, once two gates possess the same polarity, 100% spin-polarized current with reversible spin orientation can be created by altering the signs of gate voltages. In addition, the heterojunction exhibits significant negative differential resistance effect behaviors with a large peak-to-valley current ratio. These results show that the combination of cold metals and bipolar magnetic semiconductors is quite promising for making multifunctional spintronic devices with simultaneous spin valve, spin filter, and negative differential resistance functions.

ACKNOWLEDGMENTS

This paper is financially supported by the National Natural Science Foundation of China (Grants No. 22103020, No. 22273092, and No. 22322304), by the Fundamental

Research Funds for the Central Universities (Grant No. JZ2023HGTB0219), by the Strategic Priority Research Program of the Chinese Academy of Sciences (Grant No. XDB0450101), by the Youth Innovation Promotion Association CAS (Grant No. 2019441), and by USTC Tang Scholar.

- [1] K. S. Burch, D. Mandrus, and J.-G. Park, Magnetism in two-dimensional van der Waals materials, *Nature (London)* **563**, 47 (2018).
- [2] W. Han, R. K. Kawakami, M. Gmitra, and J. Fabian, Graphene spintronics, *Nat. Nanotechnol.* **9**, 794 (2014).
- [3] D. Zhong, K. L. Seyler, X. Linpeng, R. Cheng, N. Sivadas, B. Huang, E. Schmidgall, T. Taniguchi, K. Watanabe, M. A. McGuire, E. Yao, D. Xiao, K. -M. C. Fu, and X. Xu, Van der Waals engineering of ferromagnetic semiconductor heterostructures for spin and valleytronics, *Sci. Adv.* **3**, e1603113 (2017).
- [4] Q. H. Wang, A. Bedoya-Pinto, M. Blei, A. H. Dismukes, A. Hamo, S. Jenkins, M. Koperski, Y. Liu, Q.-C. Sun, E. J. Telford, H. H. Kim, M. Augustin, U. Vool, J. -X. Yin, L. H. Li, A. Falin, C. R. Dean, F. Casanova, R. F. L. Evans, M. Chshiev *et al.*, The magnetic genome of two-dimensional van der Waals materials, *ACS Nano* **16**, 6960 (2022).
- [5] Y. Deng, Y. Yu, Y. Song, J. Zhang, N. Z. Wang, Z. Sun, Y. Yi, Y. Z. Wu, S. Wu, J. Zhu, J. Wang, X. H. Chen, and Y. Zhang, Gate-tunable room-temperature ferromagnetism in two-dimensional Fe_3GeTe_2 , *Nature (London)* **563**, 94 (2018).
- [6] M. Gibertini, M. Koperski, A. F. Morpurgo, and K. S. Novoselov, Magnetic 2D materials and heterostructures, *Nat. Nanotechnol.* **14**, 408 (2019).
- [7] B. Huang, G. Clark, D. R. Klein, D. MacNeill, E. Navarro-Moratalla, K. L. Seyler, N. Wilson, M. A. McGuire, D. H. Cobden, D. Xiao, W. Yao, P. Jarillo-Herrero, and X. Xu, Electrical control of 2D magnetism in bilayer CrI_3 , *Nat. Nanotechnol.* **13**, 544 (2018).
- [8] J.-U. Lee, S. Lee, J. H. Ryoo, S. Kang, T. Y. Kim, P. Kim, C.-H. Park, J.-G. Park, and H. Cheong, Ising-type magnetic ordering in atomically thin FePS_3 , *Nano Lett.* **16**, 7433 (2016).
- [9] B. Huang, G. Clark, E. Navarro-Moratalla, D. R. Klein, R. Cheng, K. L. Seyler, D. Zhong, E. Schmidgall, M. A. McGuire, D. H. Cobden, W. Yao, D. Xiao, P. Jarillo-Herrero, and X. Xu, Layer-dependent ferromagnetism in a van der Waals crystal down to the monolayer limit, *Nature (London)* **546**, 270 (2017).
- [10] C. Gong, L. Li, Z. Li, H. Ji, A. Stern, Y. Xia, T. Cao, W. Bao, C. Wang, Y. Wang, Z. Q. Qiu, R. J. Cava, S. G. Louie, J. Xia, and X. Zhang, Discovery of intrinsic ferromagnetism in two-dimensional van der Waals crystals, *Nature (London)* **546**, 265 (2017).
- [11] D. J. O'Hara, T. Zhu, A. H. Trout, A. S. Ahmed, Y. K. Luo, C. H. Lee, M. R. Brenner, S. Rajan, J. A. Gupta, D. W. McComb, and R. K. Kawakami, Room temperature intrinsic ferromagnetism in epitaxial manganese selenide films in the monolayer limit, *Nano Lett.* **18**, 3125 (2018).
- [12] X. Li, X. Wu, Z. Li, J. Yang, and J. G. Hou, Bipolar magnetic semiconductors: a new class of spintronics materials, *Nanoscale* **4**, 5680 (2012).
- [13] X. Li and J. Yang, Bipolar magnetic materials for electrical manipulation of spin-polarization orientation, *Phys. Chem. Chem. Phys.* **15**, 15793 (2013).
- [14] X. Li and J. Yang, First-principles design of spintronics materials, *Natl. Sci. Rev.* **3**, 365 (2016).
- [15] J. Li, X. Li, and J. Yang, A review of bipolar magnetic semiconductors from theoretical aspects, *Fundam. Res.* **2**, 511 (2022).
- [16] Y. Li, J. Deng, Y.-F. Zhang, X. Jin, W.-H. Dong, J.-T. Sun, J. Pan, and S. Du, Nonvolatile electrical control of spin polarization in the 2D bipolar magnetic semiconductor VSeF , *NPJ Comput. Mater.* **9**, 50 (2023).
- [17] Y. Chen, J. Liu, Q. Sun, Y. Kawazoe, and P. Jena, Bipolar magnetic materials based on 2D Ni[TCNE] metal-organic coordination networks, *Adv. Electron. Mater.* **4**, 1700323 (2018).
- [18] Y. Ke, W. Li, G. Yin, L. Zhang, and R. Quhe, Quantum transport simulations of a proposed logic-in-memory device based on a bipolar magnetic semiconductor, *Phys. Rev. Appl.* **20**, 014050 (2023).
- [19] N. Luo, C. Si, and W. Duan, Structural and electronic phase transitions in ferromagnetic monolayer VS_2 induced by charge doping, *Phys. Rev. B* **95**, 205432 (2017).
- [20] H. Sheng, H. Long, G. Zou, D. Bai, J. Zhang, and J. Wang, Magnetic and phonon transport properties of two-dimensional room-temperature ferromagnet VSe_2 , *J. Mater. Sci.* **56**, 15844 (2021).
- [21] X. Li, X. Wu, and J. Yang, Half-metallicity in MnPSe_3 exfoliated nanosheet with carrier doping, *J. Am. Chem. Soc.* **136**, 11065 (2014).
- [22] H. Pan, Y. Sun, Y. Zheng, N. Tang, and Y. Du, B_4CN_3 and B_3CN_4 monolayers as the promising candidates for metal-free spintronic materials, *New J. Phys.* **18**, 093021 (2016).
- [23] X. Li and J. Yang, Toward room-temperature magnetic semiconductors in two-dimensional ferrimagnetic organometallic lattices, *J. Phys. Chem. Lett.* **10**, 2439 (2019).
- [24] X. Li and J. Yang, Realizing two-dimensional magnetic semiconductors with enhanced Curie temperature by antiaromatic ring based organometallic frameworks, *J. Am. Chem. Soc.* **141**, 109 (2019).
- [25] X. Li, H. Lv, X. Liu, T. Jin, X. Wu, X. Li, and J. Yang, Two-dimensional bipolar magnetic semiconductors with high Curie-temperature and electrically controllable spin polarization realized in exfoliated $\text{Cr}(\text{pyrazine})_2$ monolayers, *Sci. China Chem.* **64**, 2212 (2021).
- [26] Q. Feng, X. Li, and J. Yang, Two-dimensional multifunctional metal-organic framework with intrinsic bipolar magnetic semiconductivity and negative Poisson's ratio, *ACS Appl. Electron. Mater.* **4**, 3198 (2022).
- [27] P. Wang, X. Jiang, J. Hu, B. Wang, T. Zhou, H. Yuan, and J. Zhao, Robust spin manipulation in 2D organometallic Kagome lattices: a first-principles study, *Phys. Chem. Chem. Phys.* **22**, 11045 (2020).
- [28] X. Li, X. Li, and J. Yang, Two-dimensional multifunctional metal-organic frameworks with simultaneous ferro-/ferrimagnetism and vertical ferroelectricity, *J. Phys. Chem. Lett.* **11**, 4193 (2020).

- [29] H. Lv, X. Li, D. Wu, Y. Liu, X. Li, X. Wu, and J. Yang, Enhanced Curie temperature of two-dimensional Cr(II) aromatic heterocyclic metal-organic framework magnets via strengthened orbital hybridization, *Nano Lett.* **22**, 1573 (2022).
- [30] X. Li, Q.-B. Liu, Y. Tang, W. Li, N. Ding, Z. Liu, H.-H. Fu, S. Dong, X. Li, and J. Yang, Quintuple function integration in two-dimensional Cr(II) five-membered heterocyclic metal organic frameworks via tuning ligand spin and lattice symmetry, *J. Am. Chem. Soc.* **145**, 7869 (2023).
- [31] J. Li, X. Li, and J. Yang, Chemically controlled reversible magnetic phase transition in two-dimensional organometallic lattices, *Nano Lett.* **23**, 9126 (2023).
- [32] J. Cheng, Q. Feng, X. Li, and J. Yang, Two-dimensional robust ferromagnetic semiconductors via assembly of magnetic superatoms $[\text{Fe}_6\text{S}_8(\text{CN})_6]^{5-}$, *J. Phys. Chem. Lett.* **14**, 5048 (2023).
- [33] J. Su, M. Wang, Y. Li, F. Wang, Q. Chen, P. Luo, J. Han, S. Wang, H. Li, and T. Zhai, Sub-millimeter-scale monolayer p-type H-phase VS_2 , *Adv. Funct. Mater.* **30**, 2000240 (2020).
- [34] X. Wang, L. Ma, C. Wang, J. Wang, J. Guo, R. Tang, J. Zhu, and G. Zou, Seed engineering toward layer-regulated growth of magnetic semiconductor VS_2 , *Adv. Funct. Mater.* **33**, 2213295 (2023).
- [35] N. Jin, S.-Y. Chung, R. M. Heyns, P. R. Berger, R. Yu, P. E. Thompson, and S. L. Rommel, Tri-state logic using vertically integrated Si-SiGe resonant interband tunneling diodes with double NDR, *IEEE Electron Device Lett.* **25**, 646 (2004).
- [36] Hurst, Multiple-valued logic—Its status and its future, *IEEE Trans Comput* **100**, 1160 (1984).
- [37] J. Shim, S. Oh, D.-H. Kang, S.-H. Jo, M. H. Ali, W.-Y. Choi, K. Heo, J. Jeon, S. Lee, M. Kim, Y. J. Song, and J.-H. Park, Phosphorene/rhenium disulfide heterojunction-based negative differential resistance device for multi-valued logic, *Nat. Commun.* **7**, 13413 (2016).
- [38] B. Murugan and S. Y. Lee, Two-dimensional materials based on negative differential transconductance and negative differential resistance for the application of multi-valued logic circuit: a review, *Carbon Lett.* **33**, 59 (2023).
- [39] T. Roy, M. Tosun, X. Cao, H. Fang, D.-H. Lien, P. Zhao, Y.-Z. Chen, Y.-L. Chueh, J. Guo, and A. Javey, Dual-gated $\text{MoS}_2/\text{WSe}_2$ van der Waals tunnel diodes and transistors, *ACS Nano* **9**, 2071 (2015).
- [40] L. Esaki, New phenomenon in narrow germanium p - n junctions, *Phys. Rev.* **109**, 603 (1958).
- [41] B. Ganjipour, A. W. Dey, B. M. Borg, M. Ek, M.-E. Pistol, K. A. Dick, L.-E. Wernersson, and C. Thelander, High current density Esaki tunnel diodes based on GaSb-InAsSb heterostructure nanowires, *Nano Lett.* **11**, 4222 (2011).
- [42] L. L. Chang, L. Esaki, and R. Tsu, Resonant tunneling in semiconductor double barriers, *Appl. Phys. Lett.* **24**, 593 (1974).
- [43] C. Bayram, Z. Vashaei, and M. Razeghi, Reliability in room-temperature negative differential resistance characteristics of low-aluminum content AlGaIn/GaN double-barrier resonant tunneling diodes, *Appl. Phys. Lett.* **97**, 181109 (2010).
- [44] P. See, D. J. Paul, B. Hollander, S. Mantl, I. V. Zozoulenko, and K.-F. Berggren, High performance Si/Si $_{1-x}$ Ge $_x$ resonant tunneling diodes, *IEEE Electron Device Lett.* **22**, 182 (2001).
- [45] A. Mishchenko, J. S. Tu, Y. Cao, R. V. Gorbachev, J. R. Wallbank, M. T. Greenaway, V. E. Morozov, S. V. Morozov, M. J. Zhu, S. L. Wong, F. Withers, C. R. Woods, Y.-J. Kim, K. Watanabe, T. Taniguchi, E. E. Vdovin, O. Makarovskiy, T. M. Fromhold, V. I. Fal'ko, A. K. Geim *et al.*, Twist-controlled resonant tunnelling in graphene/boron nitride/graphene heterostructures, *Nat. Nanotechnol.* **9**, 808 (2014).
- [46] S. Montanari, A. Förster, M. I. Lepsa, and H. Lüth, High frequency investigation of graded gap injectors for GaAs Gunn diodes, *Solid-State Electron.* **49**, 245 (2005).
- [47] A. S. Hajo, O. Yilmazoglu, A. Dadgar, F. Küppers, and T. Kusserow, Reliable GaN-based THz Gunn diodes with side-contact and field-plate technologies, *IEEE Access* **8**, 84116 (2020).
- [48] C. P. Heij, D. C. Dixon, P. Hadley, and J. E. Mooij, Negative differential resistance due to single-electron switching, *Appl. Phys. Lett.* **74**, 1042 (1999).
- [49] N. Simonian, J. Li, and K. Likharev, Negative differential resistance at sequential single-electron tunnelling through atoms and molecules, *Nat. Nanotechnol.* **18**, 424006 (2007).
- [50] J. Chen, M. A. Reed, A. M. Rawlett, and J. M. Tour, Large on-off ratios and negative differential resistance in a molecular electronic device, *Science* **286**, 1550 (1999).
- [51] E. D. Mentovich, I. Kalifa, A. Tsukernik, A. Caster, N. Rosenberg-Shraga, H. Marom, M. Gozin, and S. Richter, Multiple peak negative-differential-resistance molecular device, *Small* **4**, 55 (2008).
- [52] J. Appenzeller, Y.-M. Lin, J. Knoch, and P. Avouris, Band-to-band tunneling in carbon nanotube field-effect transistors, *Phys. Rev. Lett.* **93**, 196805 (2004).
- [53] S. Gundapaneni, M. Bajaj, R. K. Pandey, K. V. M. Murali, S. Ganguly, and A. Kottantharayil, Effect of band-to-band tunneling on junctionless transistors, *IEEE Trans. Electron Devices* **59**, 1023 (2012).
- [54] G. Woo, T. Kim, and H. Yoo, Band-to-band tunneling control by external forces: A key principle and applications, *Adv. Electron. Mater.* **9**, 2201015 (2023).
- [55] A. Nourbakhsh, A. Zubair, M. S. Dresselhaus, and T. Palacios, Transport properties of a $\text{MoS}_2/\text{WSe}_2$ heterojunction transistor and its potential for application, *Nano Lett.* **16**, 1359 (2016).
- [56] S. Fan, Q. A. Vu, S. Lee, T. L. Phan, G. Han, Y.-M. Kim, W. J. Yu, and Y. H. Lee, Tunable negative differential resistance in van der Waals heterostructures at room temperature by tailoring the interface, *ACS Nano* **13**, 8193 (2019).
- [57] J. Lee, N. T. Duong, S. Bang, C. Park, D. A. Nguyen, H. Jeon, J. Jang, H. M. Oh, and M. S. Jeong, Modulation of junction modes in $\text{SnSe}_2/\text{MoTe}_2$ broken-gap van der Waals heterostructure for multifunctional devices, *Nano Lett.* **20**, 2370 (2020).
- [58] K.-H. Kim, H.-Y. Park, J. Shim, G. Shin, M. Andreev, J. Koo, G. Yoo, K. Jung, K. Heo, Y. Lee, H.-Y. Yu, K. R. Kim, J. H. Cho, S. Lee, and J.-H. Park, A multiple negative differential resistance heterojunction device and its circuit application to ternary static random access memory, *Nanoscale Horiz.* **5**, 654 (2020).
- [59] Q. Lv, F. Yan, N. Mori, W. Zhu, C. Hu, Z. R. Kudrynskiy, Z. D. Kovalyuk, A. Patanè, and K. Wang, Interlayer band-to-band tunneling and negative differential resistance in van der Waals BP/InSe field-effect transistors, *Adv. Funct. Mater.* **30**, 1910713 (2020).

- [60] R. Yan, S. Fathipour, Y. Han, B. Song, S. Xiao, M. Li, N. Ma, V. Protasenko, D. A. Muller, D. Jena, and H. G. Xing, Esaki diodes in van der Waals heterojunctions with broken-gap energy band alignment, *Nano Lett.* **15**, 5791 (2015).
- [61] H. Wang, X. Huang, J. Lin, J. Cui, Y. Chen, C. Zhu, F. Liu, Q. Zeng, J. Zhou, P. Yu, X. Wang, H. He, S. H. Tsang, W. Gao, K. Suenaga, F. Ma, C. Yang, L. Lu, T. Yu, E. H. T. Teo *et al.*, High-quality monolayer superconductor NbSe₂ grown by chemical vapour deposition, *Nat. Commun.* **8**, 394 (2017).
- [62] X. Wang, J. Lin, Y. Zhu, C. Luo, K. Suenaga, C. Cai, and L. Xie, Chemical vapor deposition of trigonal prismatic NbS₂ monolayers and 3R-polytype few-layers, *Nanoscale* **9**, 16607 (2017).
- [63] J. Shi, X. Chen, L. Zhao, Y. Gong, M. Hong, Y. Huan, Z. Zhang, P. Yang, Y. Li, Q. Zhang, Q. Zhang, L. Gu, H. Chen, J. Wang, S. Deng, N. Xu, and Y. Zhang, Chemical vapor deposition grown wafer-scale 2D tantalum diselenide with robust charge-density-wave order, *Adv. Mater.* **30**, 1804616 (2018).
- [64] J. Wu, J. Peng, Z. Yu, Y. Zhou, Y. Guo, Z. Li, Y. Lin, K. Ruan, C. Wu, and Y. Xie, Acid-assisted exfoliation toward metallic subnanopore TaS₂ monolayer with high volumetric capacitance, *J. Am. Chem. Soc.* **140**, 493 (2018).
- [65] Z. Wang, X. Xie, L. Zhang, R. Cao, X. Liu, S. Cho, and F. Liu, Cold source diodes with sub-unity ideality factor and giant negative differential resistance, *IEEE Electron Device Lett.* **43**, 2184 (2022).
- [66] Y. Yin, Z. Zhang, C. Shao, J. Robertson, and Y. Guo, Computational study of transition metal dichalcogenide cold source MOSFETs with sub-60 mV per decade and negative differential resistance effect, *npj 2D Mater. Appl.* **6**, 55 (2022).
- [67] F. Liu, Switching at less than 60 mV/decade with a “cold” metal as the injection source, *Phys. Rev. Appl.* **13**, 064037 (2020).
- [68] G. Kresse and J. Furthmüller, Efficient iterative schemes for *ab initio* total-energy calculations using a plane-wave basis set, *Phys. Rev. B* **54**, 11169 (1996).
- [69] G. Kresse and J. Furthmüller, Efficiency of *ab-initio* total energy calculations for metals and semiconductors using a plane-wave basis set, *Comput. Mater. Sci.* **6**, 15 (1996).
- [70] J. P. Perdew, K. Burke, and M. Ernzerhof, Generalized gradient approximation made simple, *Phys. Rev. Lett.* **77**, 3865 (1996).
- [71] M. Brandbyge, J.-L. Mozos, P. Ordejón, J. Taylor, and K. Stokbro, Density-functional method for nonequilibrium electron transport, *Phys. Rev. B* **65**, 165401 (2002).
- [72] J. Taylor, H. Guo, and J. Wang, *Ab initio* modeling of quantum transport properties of molecular electronic devices, *Phys. Rev. B* **63**, 245407 (2001).
- [73] M. J. van Setten, M. Giantomassi, E. Bousquet, M. J. Verstraete, D. R. Hamann, X. Gonze, and G.-M. Rignanese, The PSEUDODOJO: Training and grading a 85 element optimized norm-conserving pseudopotential table, *Comput. Phys. Commun.* **226**, 39 (2018).
- [74] S. Smidstrup, T. Markussen, P. Vancaeyveld, J. Wellendorff, J. Schneider, T. Gunst, B. Verstichel, D. Stradi, P. A. Khomyakov, U. G. Vej-Hansen, M.-E. Lee, S. T. Chill, F. Rasmussen, G. Penazzi, F. Corsetti, A. Ojanperä, K. Jensen, M. L. N. Palsgaard, U. Martinez, A. Blom *et al.*, QuantumATK: An integrated platform of electronic and atomic-scale modelling tools, *J. Phys.: Condens. Matter* **32**, 015901 (2020).
- [75] See Supplemental Material at <http://link.aps.org/supplemental/10.1103/PhysRevB.109.054428> for the details of a few theoretical results. The optimization of the heterostructure device configuration, the band structure of the 2H-VS₂ monolayer, the electrostatic potential and the projected band structure, the transmission spectra, and the spin- and spatially resolved projected local density of states under different gate and bias voltages are presented.
- [76] J. Zhou, M. Khazaei, A. Ranjbar, V. Wang, T. D. Kühne, K. Ohno, Y. Kawazoe, and Y. Liang, Modulation of nearly free electron states in hydroxyl-functionalized MXenes: a first-principles study, *J. Mater. Chem. C* **8**, 5211 (2020).
- [77] J. Yang, S. Zhang, A. Wang, R. Wang, C.-K. Wang, G.-P. Zhang, and L. Chen, High magnetoresistance in ultra-thin two-dimensional Cr-based MXenes, *Nanoscale* **10**, 19492 (2018).
- [78] K. T. Delaney, N. A. Spaldin, and C. G. Van de Walle, Theoretical study of Schottky-barrier formation at epitaxial rare-earth-metal/semiconductor interfaces, *Phys. Rev. B* **81**, 165312 (2010).
- [79] M. Aras, Ç. Kılıç, and S. Ciraci, Lateral and vertical heterostructures of transition metal dichalcogenides, *J. Phys. Chem. C* **122**, 1547 (2018).
- [80] Z. Ahangari and H. Heidari, Emerging field effect transistor architectures-part I, in *Nanoelectronics: Physics, Materials and Devices*, edited by A. Sarkar, C. K. Sarkar, A. Deyasi, D. De, and A. Benfdila, Micro and Nano Technologies (Elsevier, Amsterdam, 2023), pp. 63–93.
- [81] S.-J. Choi, C.-J. Choi, J.-Y. Kim, M. Jang, and Y.-K. Choi, Analysis of transconductance (g_m) in Schottky-barrier MOSFETs, *IEEE Trans. Electron Devices* **58**, 427 (2011).
- [82] Y. Gong, J. Lin, X. Wang, G. Shi, S. Lei, Z. Lin, X. Zou, G. Ye, R. Vajtai, B. I. Yakobson, H. Terrones, M. Terrones, B. K. Tay, J. Lou, S. T. Pantelides, Z. Liu, W. Zhou, and P. M. Ajayan, Vertical and in-plane heterostructures from WS₂/MoS₂ monolayers, *Nat. Mater.* **13**, 1135 (2014).
- [83] S. Song, A. Yoon, J.-K. Ha, J. Yang, S. Jang, C. Leblanc, J. Wang, Y. Sim, D. Jariwala, S. K. Min, Z. Lee, and S.-Y. Kwon, Atomic transistors based on seamless lateral metal-semiconductor junctions with a sub-1-nm transfer length, *Nat. Commun.* **13**, 4916 (2022).
- [84] C. Huang, S. Wu, A. M. Sanchez, J. J. P. Peters, R. Beanland, J. S. Ross, P. Rivera, W. Yao, D. H. Cobden, and X. Xu, Lateral heterojunctions within monolayer MoSe₂-WSe₂ semiconductors, *Nat. Mater.* **13**, 1096 (2014).
- [85] Y. Zhang, L. Yin, J. Chu, T. A. Shifa, J. Xia, F. Wang, Y. Wen, X. Zhan, Z. Wang, and J. He, Edge-epitaxial growth of 2D NbS₂-WS₂ lateral metal-semiconductor heterostructures, *Adv. Mater.* **30**, 1803665 (2018).